Spatio-temporal chromosomal arrangements by late-replicating heterochromatin

Satya Dev Polisetty[1], Shuvadip Dutta[2], Rakesh Netha Vadnala[3], Dimple Notani[3], Ranjith Padinhateeri[4,5,6], Kaustuv Sanyal*[1,7]

[1]Molecular Mycology Laboratory, Molecular Biology and Genetics Unit, Jawaharlal Nehru Centre for Advanced Scientific Research, Bengaluru, India.
[2]Department of Physics, Indian Institute of Technology Bombay, Mumbai, India.
[3]National Centre for Biological Sciences, TIFR, Bengaluru, India.
[4]Department of Biosciences and Bioengineering, Indian Institute of Technology Bombay, Mumbai, India.
[5]Sunita Sanghi Centre of Aging and Neurodegenerative Diseases, Indian Institute of Technology Bombay, Mumbai, India.
[6] Koita Centre for Digital Health, Indian Institute of Technology Bombay, Powai, Mumbai, 400076, India
[7]Department of Biological Sciences, Bose Institute, Kolkata, India.

*sanyal@jncasr.ac.in, sanyal@jcbose.ac.in

Summary
Centromere clustering orchestrates the three-dimensional genome organization and, in turn, impacts genome stability[1-4]. In this study, we report the principles governing the chromosome-scale architectural changes associated with centromere clustering and declustering in *Cryptococcus neoformans,* an opportunistic human fungal pathogen. We demonstrate that centromeres and telomeres in *C. neoformans* are scattered around the nuclear periphery during interphase[G1], resembling metazoans rather than model budding yeasts. Hi-C data of the synchronised cells reveal centromere and telomere-associated heterochromatic regions are organized as separate compartments at the nuclear periphery, distinct from the euchromatic regions, that eventually shape the global organization of interphase[G1] chromosomes. Polymer modeling of the Hi-C data at interphase and anaphase stages strongly supports a global reorganization of chromosomes from the non-Rabl to the Rabl-like chromosomal arrangement. Most strikingly, while centromeres are clustered and replicate early in most yeasts, our sort-seq studies provide evidence that *C. neoformans* centromeres replicate late during the S-phase. In summary, we uncover yet unknown principles governing the chromosome-scale architecture that link centromere DNA replication timing, spatial centromere positioning, functional compartmentalization of chromosomes, and dynamic changes in the global three-dimensional genome architecture in a species that shared a common ancestor with metazoans more than a billion years ago.

Introduction
Chromosomes in a eukaryotic cell are three-dimensionally organized in two recurring configurations based on the spatial positioning of centromeres and telomeres[5], Rabl and non-Rabl/Type-II. In the Rabl configuration, centromeres and telomeres are spatially separated within the nucleus and arranged in separate clusters. The clustered centromeres and the telomere cluster are located at the nuclear periphery, but these two clusters are spatially positioned on opposite ends of the nucleus. In contrast, the non-Rabl/type-II configuration is marked by the territorial arrangement of chromosomes, where individual centromeres and telomeres are scattered across the nucleus, sometimes forming subclusters. Well-studied fungi in the phylum of Ascomycota show the Rabl arrangement of chromosomes[6], but most metazoan chromosomes tend to adopt the non-Rabl configuration[6]. Strikingly, *Schizosaccharomyces pombe* and *Magnaporthe oryzae* genomes adopt the Rabl arrangement[7,8] except transient declustering of centromeres is observed at metaphase. In the fruit fly *Drosophila melanogaster,* the centromere clustering is developmental stage-specific. While chromosomes in embryonic nuclei display the Rabl configuration[9] with clustered centromeres, more differentiated fly cells, such as spermatocytes[10] have unclustered centromeres as chromosomes adopt the non-Rabl organization. Metazoans, including humans, exhibit differentiation-specific clustering of centromeres with the nucleolus, which is lost in terminally differentiated cells[11]. Intriguingly, centromeres show a strong propensity to cluster around the nucleolus in human cancer cells[11] although the role of centromere clustering in cancer cells needs to be explored.

Apart from shaping the chromosome-scale architecture, spatial positioning and clustering of centromeres impact the regulation of several structural aspects of the genome, including the telomere bouquet formation during meiosis in *S. pombe*[12]. While the importance of centromere clustering in shaping the genome architecture and function is significant, functional and architectural differences involved in clustered and unclustered centromere states are underappreciated. In this study, we report that in the basidiomycete budding yeast,

Cryptococcus neoformans[13], the centromere clustering states differ according to the cell cycle stages - centromeres are unclustered during interphase and gradually cluster during mitosis[13]. This unique feature of dynamic changes in chromosomal organization makes *C. neoformans* an attractive model to track the natural transition of two major chromosome arrangements that exist across species. While the spatial positioning of centromeres orchestrates the overall three-dimensional genome organization[3], *C. neoformans* holds the key to link chromosome architectural changes associated with centromere clustering during the mitotic cell cycle.

Switching between non-Rabl and Rabl

The cell cycle stage-dependent spatial clustering of centromeres/kinetochores has already been reported in *C. neoformans*[13,14]. We identified the homolog of Protector of Telomeres (Pot1), a single-strand telomere DNA binding protein[15] (Extended Data Fig. 1) in *C. neoformans*. GFP-Pot1 was expressed in a strain where centromeres were marked with mCherry-tagged CENP-A. Telomeres in G1 cells were visible as multiple puncta located at the nuclear periphery, similar to centromeres (Fig. 1a), unlike any polarized distribution observed in *Saccharomyces cerevisiae* or *S. pombe*[16-18]. Instead, centromeres and telomeres in *C. neoformans* show no prominent spatial clustering resembling interphase cells of metazoans such as humans[19]. Centromeres in *C. neoformans* appear to cluster during G2 and anaphase as chromosomes adopt the Rabl-like arrangement (Fig. 1a and b), typically observed in yeast species. While there are 14 chromosomes in *C. neoformans,* the number of telomere puncta observed in G1 cells is significantly less than 28, indicating telomeres form subclusters (Fig. 1c). We could not detect Pot1 signals in most metaphase cells when centromeres migrated into the daughter bud. Notably, while centromeres do not form a single punctum, 14 individual centromere puncta in each G1 cell could not be detected, indicating centromeres form subclusters[13]. To further resolve the spatial positions of centromeres and telomeres, we imaged cells using 3D Structured Illumination Microscopy (SIM[2]) (Fig. 1d). This approach revealed that centromeres and telomeres are indeed scattered across the nucleus and occupy non-overlapping spatially proximal positions in interphase[G1] cells.

Telomere interactions dominate G1 genome

To study the cell cycle-associated changes in the genome organization of the *H99* strain of *C. neoformans*, we performed Hi-C in synchronized interphase[G1] and mitotic cells at metaphase and anaphase (Extended Data Fig. 2 a, b and c), and generated whole genome contact maps (Fig. 1e). Hi-C was performed in two replicates at each of these stages. To assess the reproducibility of Hi-C data sets, we calculated pair-wise Pearson correlation coefficients of the datasets binned at 8 kb. The results indicate high concordance among the biological replicates (Extended Data Fig. 2d).

A striking feature of contact maps of a genome with the Rabl configuration of chromosomes is the presence of strong inter-centromere interactions[20-22]. Centromeres in *C. neoformans* are regional and span between 21 to 64 kb[23]. Inspection of Hi-C maps from synchronized interphase[G1], metaphase, and anaphase cells of *C. neoformans* (Fig. 1e and f) reveals that features of the interphase[G1] contact map are distinct from those of ascomycete yeasts possessing the constitutive Rabl organization[6]. Contact maps confirm that interphase[G1] cells lack usual strong centromere interactions between the chromosomes, suggesting the non-Rabl metazoan-like chromosome arrangement (Fig. 1e, red squares and 1f and Extended Data Fig. 3a) in a fungal cell. In fact, inter-telomere interactions across the chromosomes are

strongly enriched (Fig. 1e, green squares and 1f and Extended Data Fig. 3a). Such telomere-telomere interactions significantly reduce at metaphase, possibly due to chromatin compaction. The telomere interactions associated with left and right arms of the chromosomes remained uniform across stages (Fig. 1f, Extended Data Fig. 3a). While microscopic observations demonstrate the existence of multiple telomere puncta, Hi-C data support enriched telomere contacts, confirming subclustering of telomeres during interphase^{G1}, and anaphase. Perhaps the subcluster composition of telomeres is heterogeneous at the single cell level, which explains prominent telomere-telomere interactions in contact maps since Hi-C contacts are population averages. The metaphase stage in *C. neoformans* is characterized by a modest increase in inter-centromeric interactions as compared to interphase^{G1}, consistent with microscopy results where centromeres appear to be loosely clustered and stretched along the spindle during metaphase[13]. Hi-C data reveal that anaphase cells of *C. neoformans* exhibit features similar to the Rabl configuration, characterized by the strongest *trans*-chromosomal interactions mediated by centromeres as well as telomeres (Fig. 1e and f, Extended Data Fig. 3a).

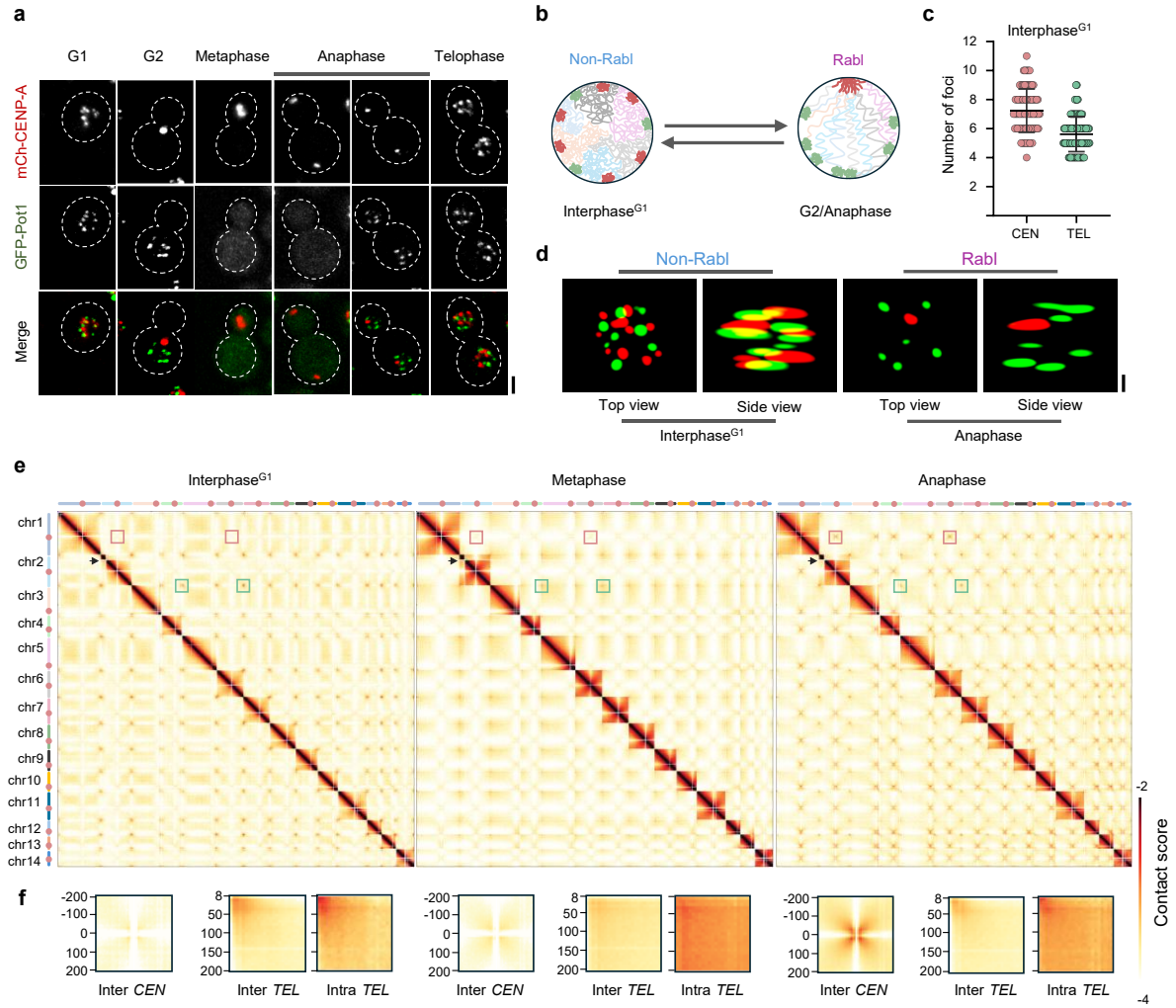

Fig. 1: The *C. neoformans* genome alternates between the non-Rabl and Rabl configurations during the cell cycle. a, Microscopic images of centromeres and telomeres marked by mCherry-CENP-A and GFP-Pot1, respectively, at different cell cycle stages. Scale bar, 2 μm. **b,** Schematic of the non-Rabl and Rabl arrangement of chromosomes. **c**, Quantification of the number of centromere or telomere puncta in interphase^{G1} stage, n=90

cells. **d**, 3D rendering of microscopic images of centromeres and telomeres of indicated cell cycle stages, Scale bar, 0.5 µm. **e**, Whole genome contact maps of interphase^{G1}, metaphase, and anaphase stages binned at 8 kb resolution. Chromosomes with centromeres marked in red circles are displayed on the left and at the top of the contact maps. Red and green squares on the maps represent inter-centromere and inter-telomere interactions, respectively. The black arrow marks the ribosomal DNA (rDNA) locus on chromosome 2. **f**, Aggregate Hi-C maps of inter-centromere/telomere and intra-telomere interactions (between left and right arms of the same chromosome), binned at 8 kb resolution, of all chromosomes. For calculating inter-/intra-telomere contacts, the left arm of the chromosomes was used. The color scale from yellow to brown represents low to high contact scores (log_{10}), respectively. e and f panels share the same color scale.

CEN and *TEL* shape chromatin organization

Having established that *C. neoformans* chromosomes could adopt both the non-Rabl and Rabl-like arrangements in a cell cycle stage-specific manner, we sought to explore changes in the chromosomal organization facilitating the transition. A comparison of percent *cis* versus *trans* contacts across cell cycle stages reveals that the majority of interactions in interphase^{G1} chromosome are *cis*, restricted within the same chromosome as less than 20% of the contacts across the chromosomes were between different chromosomes (*trans*) (Extended Data Fig. 3b). On the other hand, metaphase and anaphase chromosomes exhibit a modest increase in *trans* contacts as compared to interphase^{G1} (Extended Data Fig. 3b). To visualize the differences in chromatin contacts across stages, we plotted observed/expected maps (Fig. 2a). A comparison of contact maps across stages identifies that pericentromeric regions are refractory to interact with the rest of the chromosome (Fig. 2a, solid ovals), a feature conserved in budding and fission yeasts[21,22]. Notably, subtelomeric regions at interphase^{G1} also behaved similar to centromeres (Fig. 2a, dashed ovals). This indicates the refractory nature of both pericentromeric and subtelomeric regions constrain the inter-/intra-arm interactions, thus shaping the non-Rabl interphase^{G1} chromosome organization (Fig. 2a, below). Unlike interphase^{G1}, subtelomeric regions at anaphase engage in extensive interactions with the arms of the same chromosome (Fig. 2a, dashed oval). Across the stages, interactions among the arms of a chromosome increased as the distance from the centromeres increased (Fig. 2a, black box). The arm-arm interactions originating from centromeres are more enriched at metaphase and anaphase, implying the folding of arms at centromeres (Fig. 2a, below). Such arm-arm interactions adjacent to centromeres are absent in the interphase^{G1} genome. Centromere-centered aggregate maps across stages yield a similar trend (Fig. 2b, black boxes). These differences further confirm that the folding of metaphase and anaphase chromosomes resembles the properties of chromosomes arranged in the Rabl form. These aggregate maps also indicate that the pericentromeric interactions within the arms are stronger in interphase^{G1} as compared to anaphase (Fig. 2b, dashed ovals), revealing these regions are highly compacted in interphase^{G1}. In metaphase, the overall increase in interactions around centromeres may be due to compaction of chromatin in general. To test if the stage-dependent compaction changes are restricted only to pericentromeric regions, we analyzed aggregate profiles of telomeres belonging to the left arm and noticed that interactions along the diagonal remains similar across the stages (Extended Data Fig. 4). To confirm these observations, we plotted average compaction profiles for individual chromosomes across stages (Fig. 2c and Extended Data Fig. 5). Note that the compaction profiles highlight the extent of local compaction within a specific chromosome and thus a comparison across different Hi-C experiments may not be appropriate. We observed that the regions flanking centromeres are highly compacted as

compared to the rest of the chromosome in interphase^{G1} and metaphase. Surprisingly, the extent of compaction of these regions at anaphase is on par with the chromosome compaction levels. In all three stages, namely interphase^{G1}, metaphase, and anaphase, telomeres remained highly compacted.

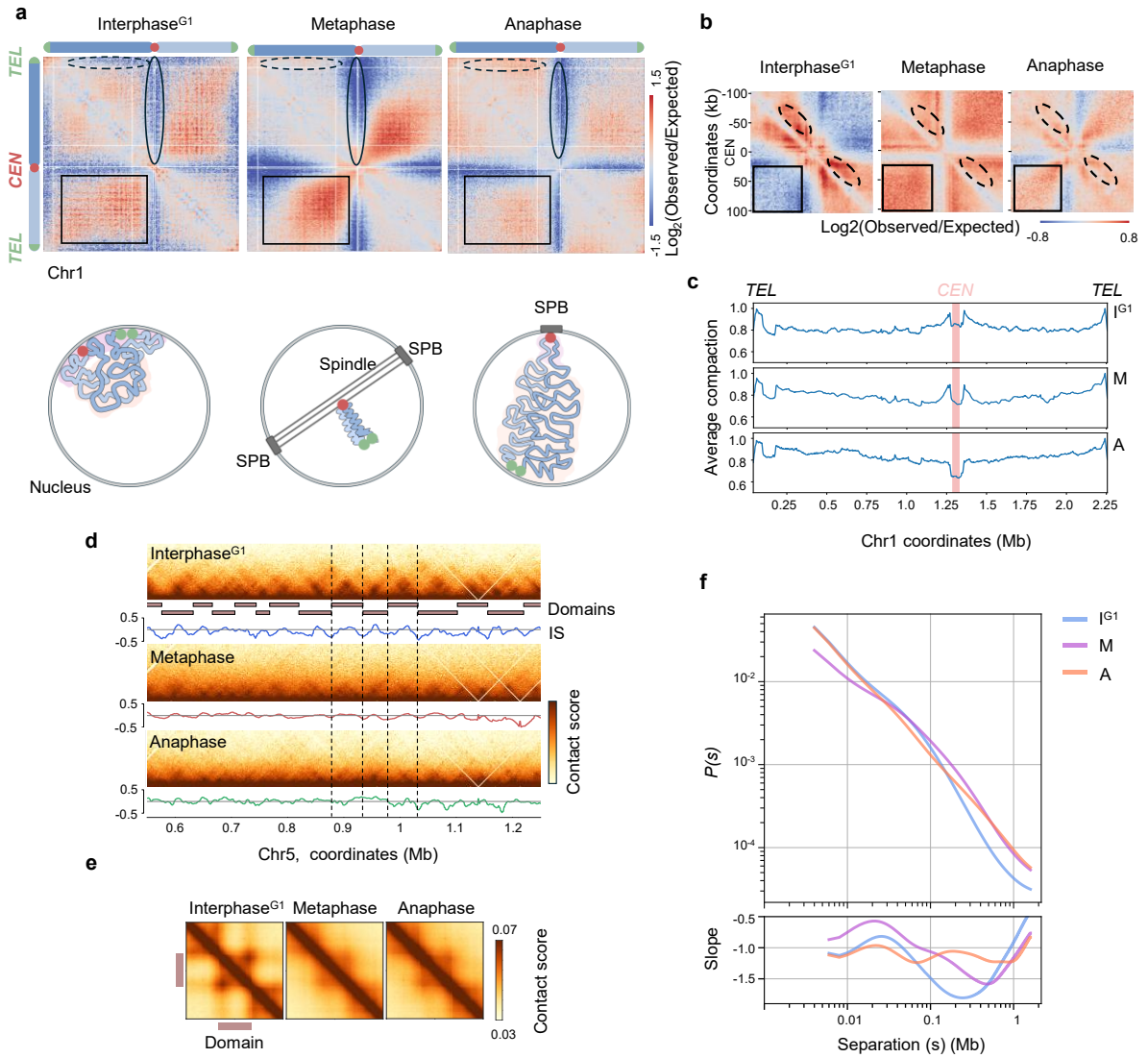

Fig. 2: Transition from the non-RabI to RabI configuration involves global chromatin decompaction. a, *Top,* Comparison of observed/expected maps of chromosome 1 of interphase^{G1}, metaphase, and anaphase stages, binned at 8 kb resolution. The blue to red color scale represents depletion and enrichment of contacts, respectively ($\log_2$ scale). Solid and dashed ovals on the maps denote the pericentromeric and subtelomeric regions, respectively. Black boxes highlight inter-arm interactions within a chromosome. *Below*, schematic highlighting structural changes in the chromosome organization across interphase^{G1}, metaphase, and anaphase stages. **b**, Observed/expected aggregate Hi-C maps of *cis*-contacts around 100 kb regions, surrounding all 14 centromeres, binned at 2 kb. Color scale as indicated above. Dashed ovals represent contacts within the arms of the chromosomes around centromeres. Black boxes represent inter-arm interactions around centromeres. **c**, Compaction profiles of chromosome 1 for the indicated stages. The x-axis represents chromosome coordinates, and the y-axis represents average compaction. The red-shaded rectangle highlights the centromere position. **d**, A region of chromosome 5 Hi-C contact map (binned at 2 kb) of interphase^{G1}, metaphase, and anaphase stages. Solid bars below interphase^{G1} contact map represent domains identified using interphase^{G1} Hi-C data.

Insulation scores (IS) are indicated below each contact map. Dotted lines represent domain boundaries. The color scale from yellow to brown represents low to high contact scores, respectively (log_{10}). **e**, Aggregate maps of domains across the three cell cycle stages (binned at 2 kb). The coordinates of the domain boundaries predicted using interphase^{G1} Hi-C data were used to generate the aggregate maps of metaphase and anaphase. **f**, *Top,* contact frequency *P(s)* curves plot of Hi-C data obtained from interphase^{G1}, metaphase, and anaphase binned at 2 kb. *Below,* derivatives (d log P(s)/d log(s)) of the *P(s)* curves.

Next, we studied the differences in local chromatin packing across the cell cycle stages. Visual inspection of Hi-C maps at 2 kb resolution indicated the presence of strong self-interacting domains, similar to the domains reported in fission yeast[21], in interphase^{G1} (Fig. 2d), To quantify changes in the domain organization, we determined domain boundaries by estimating genome-wide insulation scores[24] from interphase^{G1} Hi-C data and generated aggregate Hi-C maps of identified domains (Fig. 2e). The analysis revealed the presence 40-70 kb long domain-like structures in interphase^{G1} chromosomes (Extended Data Fig. 6). The presence of these domains was significantly reduced during metaphase, likely due to the overall compaction of chromosomes. Such domains started to appear during anaphase, hinting at the gradual reestablishment of domain-like structures, a phenomenon observed in humans[25]. The striking resemblance of the disappearance of the domain-like structure across kingdoms of life is noteworthy. Based on these observations, we suggest that local as well as global chromatin architecture and the spatial positioning of centromeres and telomeres shape the cell cycle stage-specific chromosome reorganization.

To understand the difference in the nature of chromatin folding across mitotic stages, we plotted intra-arm contact probability (*P*) over the genomic distance, *s*. *P(s)* values change in a cell cycle stage-specific manner[26]. A power-law scaling between s^{-1} and $s^{-1.5}$ indicates a fractal globule, and above $s^{-1.5}$ indicates an equilibrium globule. The *P(s)* of interphase^{G1} uncovered two regimes of power-law scaling. Regions ranging from 10 to 100 kb exhibited $\sim s^{-0.93}$ and those above 100 kb showed $s^{-1.72}$ (Fig. 2f, below and Extended Data Fig. 7a). The observed power-law scaling during interphase^{G1} in *C. neoformans* indicates that at distances <100 kb, chromatin is organized as a fractal globule, and at >100 kb, chromatin exhibits the properties of an unconstrained polymer. The metaphase stage has a slower rate of decay at distances <100 kb with a power law scaling of $s^{-0.62}$, indicating compaction of the chromosomes, and >100 kb, the decay was rapid with $\sim s^{-1.31}$ (Fig. 2f, below and Extended Data Fig. 7a), which is similar to metazoan metaphase chromosomes[26]. Anaphase chromatin, rather strikingly, showed a uniform steep decay in contact frequency with values s^{-1} and $s^{-1.1}$ for short and long distances, respectively (Fig. 2f, below and Extended Data Fig. 7a). This suggests that both at short and long distances, chromatin is folded as a fractal globule. The above-mentioned features were observed for the arms of individual chromosomes as well (Extended Data Fig. 7b-d). A comparison of interphase^{G1} and anaphase *P(s)* curves reveals that contacts between regions spanning 20-100 kb are enriched in interphase^{G1}, and the interphase^{G1} domains are of sizes 40-70 kb. We speculate that the loss of contacts at 20-100 kb distances (Fig. 2f) perhaps corresponds to the observed loss of strong domain-like structures in anaphase (Fig. 2e). On the other hand, contacts spanning ~ 150 kb are enriched in anaphase, providing an explanation for the observed increase in long-range contacts that encompass subtelomeric regions evident from O/E maps. To further confirm that anaphase chromosomes indeed exhibit enhanced distal/long-range contacts, we plotted the Distal Contact Index (DCI). DCI quantifies the ratio between distal and local contact strengths, providing a measure of the extent of long-range chromatin interactions. DCI analysis revealed

an enrichment of distal contacts >70 kb across all chromosomes during anaphase as compared to interphase^{G1} (Extended Data Fig. 8a and b). The differences in the domain organization in interphase^{G1} and anaphase stages, combined with the changes in the decay pattern of *P(s)* curves, confirm that anaphase chromatin is less compact than interphase^{G1} with reduced short-range interactions but more prominent long-range interactions.

Compartment-like features of G1 genome

Since the pericentromeres and subtelomeres are refractory to interacting with the rest of the genome, we generated a correlation matrix[27] to test if these regions behave similarly to the A and B compartments observed in metazoans[27-31]. Though we did not observe a plaid pattern that is present in metazoan contact maps[27], we noticed that both pericentromeric and subtelomeric regions in *C. neoformans* remained in one compartment, referred to as the centromere-telomere (CT) compartment, and the rest of the chromosome remained in the non-CT compartment (Fig. 3a, left panel). This pattern was lost at anaphase, where only pericentromeric regions are segregated from the rest of the genome (Fig. 3a, right panel). Next, we performed eigendecomposition[27] and the first eigen vector was used to estimate the positions of the compartments. The principal component (PC1) indicated the presence of two large compartment-like structures in all chromosomes, except for chromosomes 2 and 12. The CT compartments were enriched with H3K9me2 and H3K27me3 marks and have reduced transcription (Fig. 3b and c, Extended Data Fig. 9). To find out if these CT compartments physically interact among each other, we plotted interactions whose $\log_2$ observed/expected ratio is >3 using circos (Fig. 3b). Indeed, strong interactions were detected between subtelomeric regions of different chromosomes within the CT compartment but not with centromeres. These observations demonstrate that the *C. neoformans* interphase^{G1} genome is explicitly organized into two large euchromatic and heterochromatic compartments.

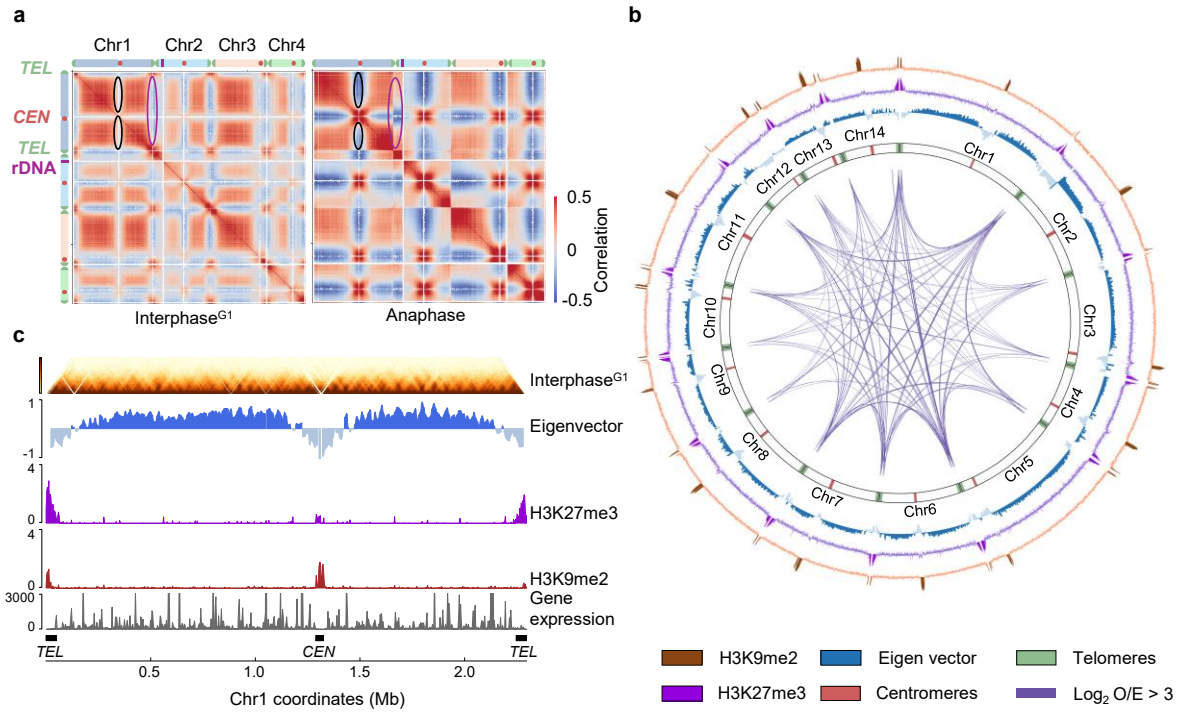

Fig. 3: Two-compartment-like organization of the *C. neoformans* interphase^{G1} genome. a, Correlation matrix of contacts for chromosomes 1 – 4 in interphase^{G1} and anaphase stages,

binned at 8 kb. The color map from blue to red represents negative to positive correlation values. Black and violet ovals represent pericentromeric and subtelomeric compartments. **b**, Circular (circos) plot representing the interactions across the subtelomeric regions and the associated chromatin modifications and eigenvector. Violet links represent the strongest inter-chromosomal contacts whose $\log_2$ (observed/expected) values are greater than 3. From outside to inside: H3K9me2 (brown), H3K27me3 (violet), eigenvector (blue), chromosomes marked with centromere (red) and telomeres (green) positions. **c**, Hi-C contact map of chromosome 1 binned at 2 kb at interphase[G1], corresponding tracks representing eigenvector, $\log_2$ ChIP enrichment profiles of H3K27me3, H3K9me2, and gene expression levels are indicated below. Black bars represent centromeres and telomeres of chromosome 1. The color scale from yellow to brown represents low to high contact scores, respectively ($\log_{10}$).

Modeling chromatin architectural changes

To better understand the overall 3D folding features of the chromosomes in Rabl and non-Rabl states, we developed a polymer model by coarse-graining the *Cryptococcus* genome into 14 flexible chains made of beads connected by springs, each representing one chromosome. Each bead represents a 10 kb chromatin segment, which is equivalent to about

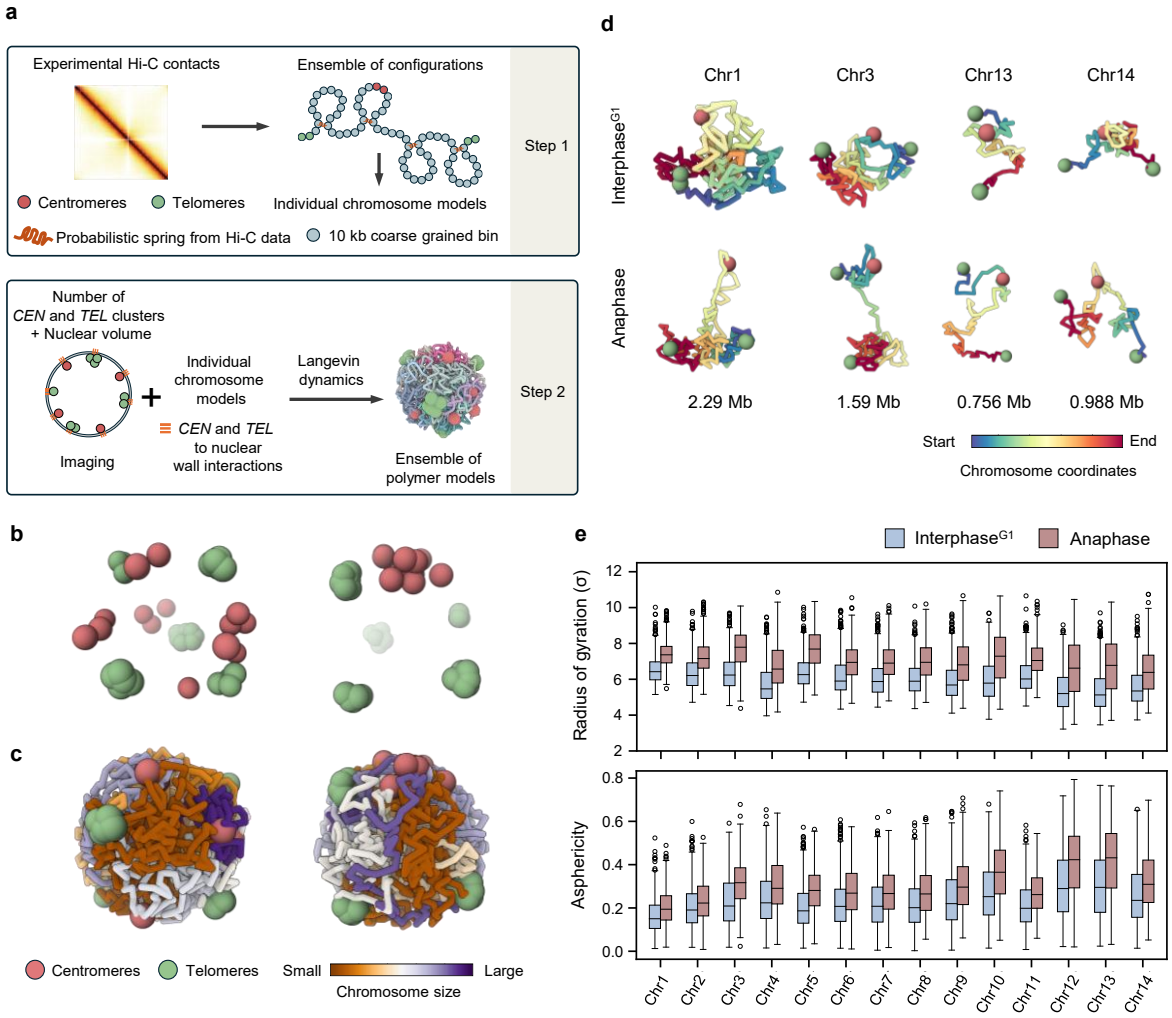

Fig. 4: Polymer modeling of the *C. neoformans* genome. a, Schematic of the steps followed for generating a polymer model of the *C. neoformans* genome. **b**, Representative snapshot of simulations of interphase[G1] and anaphase, highlighting only the spatial distributions of centromeres and telomeres. **c**, Snapshot of interphase[G1] and anaphase whole

genome polymer models. The individual chromosomes are colored according to increasing chromosome sizes. **d**, Snapshots of the polymer models of large (chr1; metacentric and chr3; acrocentric) and small (chr13; acrocentric and chr14; metacentric) chromosomes from interphase^{G1} and anaphase stages, colored from one end to the other (start to end coordinates). **e**, *Top,* Box plots of radius of gyration (R_g) values of chromosomes at interphase^{G1} and anaphase. The higher the value, the more elongated the structure. *Below,* box plots of asphericity values estimated from the polymer models of chromosomes at the indicated stages. The lesser the value, the more globular the structures. The horizontal line inside the box represents the median, and the box denotes the interquartile range, 25% to 75%.

50 nucleosomes. The polymer models were built in two sequential stages (Fig. 4a) to progressively reconstruct the global 3D genome organization. First, we generated an ensemble of individual chromosome conformations guided by Hi-C data. Next, chromosome-wise conformation states, the number of centromere and telomere clusters, and the nuclear volume were integrated to simulate the whole genome by placing all 14 chromosomes within a spherical confinement, mimicking the physical boundaries of the nucleus. Physical constraints due to stage-specific clustering of centromeres and telomeres (Fig. 4b) were introduced based on microscopy data (Fig. 1a). Visual inspection of the polymer models revealed that interphase^{G1} chromosomes form compact globular structures, whereas anaphase chromosomes are axially elongated and less compact (Fig. 4c and d). Features of anaphase chromosomes are more Rabl-like (Fig. 4d). Intriguingly, during anaphase, regions surrounding centromeres of chromosomes appeared to be more elongated as compared to interphase^{G1}. Perhaps, the axial elongation of pericentromeric regions facilitates clustering of centromeres of different chromosomes in a confined nuclear space. To quantify these changes, we estimated the radius of gyration (R_g) and asphericity (Fig. 4e) of polymer models of individual chromosomes at both stages. Interphase^{G1} chromosomes exhibited lower R_g and asphericity values, indicating more globular properties at interphase^{G1} than at anaphase. Thus, the polymer modeling helped us conclude that the shift from the non-Rabl configuration to the Rabl-type is associated with large-scale restructuring of chromosome organization.

CT compartment replicates late

The spatial proximity of centromeres and telomeres and their compartmentalization from the rest of the genome during interphase^{G1} prompted us to test whether the genome is organized according to DNA replication timing as well. Several studies suggest a link between the 3D genome architecture and DNA replication timing[2]. Various parts of a genome are replicated at different time intervals within the S-phase. To estimate replication timing, we used sort-seq[32,33] to measure the DNA copy number changes in replicating (S) cells relative to the non-replicating cells (G1). While in G1, the DNA copy number remains uniform, the copy number of different parts of the genome differs at S phase depending on the time of replication. Using this approach, we generated replication timing profiles of all 14 chromosomes of *C. neoformans* (Fig. 5a). A z-score >0 (methods) indicates early replicating and <0 indicates late replicating genomic segments. Centromeres and their flanks showed a dip in z-score values compared to other genomic regions. Similarly, subtelomeric regions (50 kb from the ends[34]) also exhibited a dip. These results helped us conclude that both centromeres and telomeres are late replicating, unlike the ascomycete fungi such as *S. cerevisiae*, *S. pombe,* and *Candida albicans*[35-37], where centromeres are one of the earliest replicating regions, and telomeres replicate late in S phase. These observations, although unexpected, establish that the replication timing of centromeres and telomeres in *C. neoformans* is similar to metazoans[38,39]

rather than the yeast species analyzed to date. Next, we investigated if the early and late replicating regions fall within two different genomic compartments that were identified earlier.

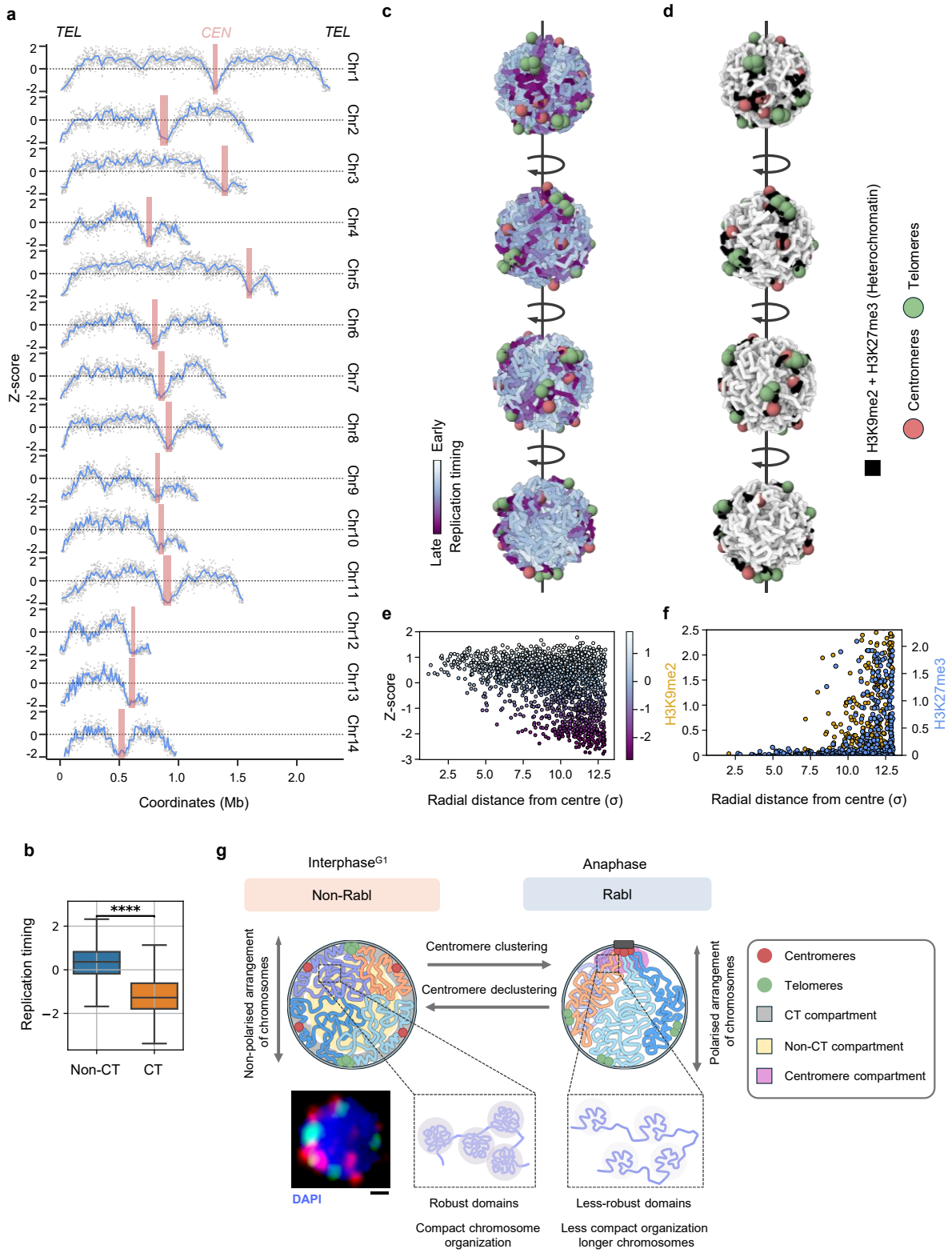

Fig. 5: Late replicating heterochromatic regions are located at the nuclear periphery, insulated from the rest of the genome. a, DNA replication profile of all fourteen chromosomes. Red shaded boxes indicate centromeric regions. The x-axis represents chromosome coordinates in Mb, and the y-axis represents the z-score. Values >0 indicate early replication, and values <0 indicate late replication. Gray dots represent 1 kb bins. The

blue line represents LOESS-smoothed z-score values. **b**, Box plot of z-score values (replication timing) of the indicated compartments. The Wilcoxon rank-sum test was used to check the significance. **c-d**, Representative snapshot of the polymer simulation of interphase^{G1} genome overlaid with, (**c**) the replication timing (z-score) values and, (**d**) the heterochromatin marks H3K9me2 and H3K27me3. Different views of the same structure are shown. The green and red spheres represent centromeres and telomeres, respectively. The blue-purple color gradient represents early to late replication timing. **e-f**, Scatter plot depicting the radial distance of the 10 kb beads of the polymer model from the center of the nucleus to the periphery with (**e**) replication timing and (**f**) ChIP enrichment profiles (log_2 values) of H3K9me2 and H3K27me3 superimposed onto the beads. **g,** Model summarizing the changes associated with the reorganization of the genome during the shift between Rabl and non-Rabl states. In the model, a microscopy image of interphase^{G1} nucleus stained with DNA-binding dye DAPI and centromere and telomeres labelled with CENPA-mCherry and GFP-Pot1. Scale bar, 1 μm.

Indeed, the late replicating regions are found to be associated with CT compartments (Fig. 5b), and the early replicating regions belong to non-CT compartments. These observations provide experimental support that both physical and functional properties/states of chromatin dictate the interphase^{G1} genome organization. Next, we investigated if the observed late-replicating regions and heterochromatin are positioned towards the periphery of the nucleus. We mapped the replication timing (z-score) values and the ChIP enrichment values of genome-wide heterochromatin marks on the polymer model. This analysis revealed that most late-replicating and heterochromatic regions are positioned towards the periphery (Fig. 5c, d, e and f and Supplementary Videos 1 and 2). This was unlike what was reported in budding yeast, where a “replication wave” like structure[40] is proposed to be present in which heterochromatic regions such as centromeres are enriched with early firing origins and telomeres are enriched with late firing origins that are arranged in a polarised fashion.

Discussion

Here we report the 3D genome organization and DNA replication timing of the human pathogenic fungus *C. neoformans*. Using Hi-C, microscopy, and polymer modeling approaches, we provide evidence that the *C. neoformans* genome dynamically switches between two major chromosome configurations, the non-Rabl and Rabl, during the cell cycle. Our results demonstrate spatial positioning of centromeres and telomeres influences the overall organization of the chromosomes. Microscopic observations confirm that interphase^{G1} chromosomes in *C. neoformans* adopt the non-Rabl arrangement as centromeres and telomeres, occupy spatially proximal positions at the nuclear periphery (Fig. 5g). This is in striking contrast to the Rabl configuration observed in most ascomycete yeasts[16-18,20,41-44]. We show that centromeres dynamically cluster and decluster during the cell cycle, whereas telomeres remain in subclusters all throughout. The Hi-C data strongly support the previously reported microscopic observation[13] that the centromeres gradually cluster in *C. neoformans* during the cell cycle progression. Interphase^{G1} Hi-C data indicate that pericentromeric and subtelomeric regions form separate CT compartments and avoid interactions with the rest of the genome. As a result, an interphase^{G1} chromosome is organized into three distinct blocks: a) euchromatin, b) the telomere block, and c) the centromere block. Centromere and telomere blocks constrain the overall organization of the interphase^{G1} chromosome by acting as an insulator. Though heterochromatin and euchromatin are well segregated in fungi[21,22], the above mode of arrangement is unique in fungi studied so far. As expected, chromosomes undergo a dramatic reorganization as interphase^{G1} chromosomes transit from the non-Rabl to the Rabl-like configuration. In anaphase, only pericentromeric compartments exist, and the

subtelomeric regions engage in long-range interactions with the arms of the chromosomes. Perhaps the polarised arrangement of centromeres and telomeres in the Rabl configuration masks the insulator effect of telomeres. The pericentromeric regions of anaphase are decondensed as compared to the rest of the genome. This is intriguing as in *S. pombe,* heterochromatin factors compact pericentromeric regions and promote inter-arm interactions between pericentromeric regions[21]. It will be interesting to investigate if the loss of pericentromere compaction promotes centromere clustering during anaphase in *C. neoformans*. Though there are differences in global chromosome organization, locally, chromatin in interphase[G1] is folded into strong self-interacting domain-like structures reported in *S. cerevisiae*, *S. pombe,* and *V. dahliae*[21,43,45]. The local chromatin organization also significantly differs between interphase[G1] and anaphase in *C. neoformans*. As expected, the robust domain-like structures apparent in interphase[G1] disappear in metaphase owing to compaction. On the other hand, these domain-like structures are reestablished during the transition from anaphase to interphase[G1] of the next cell cycle.

A comparative study across several species of eukaryotes revealed that condensin II plays an important role in shaping the genome architecture across different species[5]. The presence of both condensin I and II promotes type-II/non-Rabl configuration, where chromosomes form territories. Most fungi lack condensin II subunits and thus favor the Rabl configuration[5]. Though *C. neoformans* lacks condensin II subunits, it can organize its chromosomes in a non-Rabl configuration. A recent study in *Arabidopsis thaliana*[1] reported that condensin II and the linker of the nucleoskeleton and cytoskeleton (LINC) complex proteins help establish the non-Rabl configuration in interphase cells after exiting from mitosis. It has been shown in *C. neoformans*[13,46] that both microtubules and a LINC complex protein, Sad1, are required for timely centromere clustering. Similarly, the cytoskeleton may regulate the clustering and declustering of centromeres, and to accommodate these dynamic changes, chromatin alters its folding properties independent of condensin II. Condensin II has been repeatedly gained or lost across many eukaryotic lineages[47]. Perhaps the presence of condensin II locks the genome in type II configuration, and its loss offers flexibility to change the genome organization to suit the needs of an organism.

In this study, we also provide evidence that, like other organisms, telomeres and subtelomeric regions are late replicating in *C. neoformans*. Whereas, unlike other yeasts studied, centromeres are late replicating. Late replicating centromere and telomere regions occupy spatially proximal positions (Fig. 5c and g) and are spatially sequestered as separate compartments from the relatively early replicating euchromatic regions, in contrast to the Rabl configuration of most budding yeasts. This raises the question of whether the relative position of centromeres with respect to that of telomeres within the nucleus influences centromere replication timing in general. For example, in *S. pombe*, chromosomes are arranged in the Rabl configuration, and centromeres bind to Swi6/HP1 and recruit DDK[48], causing centromeres and their proximal regions to replicate early despite being heterochromatic. Meanwhile, at telomeres, the presence of PP1 phosphatase creates conditions that are refractory for the initiation of replication[49]. As a result, both centromeres and telomeres are present in different microenvironments that influence their replication timing[49,50]. Forced tethering of DDK to sub-telomeres did not advance the replication timing of telomeres like that of pericentromeric regions, suggesting that telomeric chromatin can hinder the recruitment of replication factors and delay its early replication[48,51]. Similarly, in *C. albicans*, a replication initiation protein Orc4 is enriched at the centromere cluster, and its concentration gradually

reduces towards the telomeres. This proposed Orc4 gradient may, in principle, create conditions contributing to early and late firing of centromeres and telomeres associated origins respectively[52]. We hypothesize that telomeres may create an environment that promotes late replication of regions associated with them. In the Rabl configuration, centromeres are spatially separated from telomeres, whereas in non-Rabl, as observed in *C. neoformans,* the proximity of centromeres to telomeres may hinder early replication of centromeres. To verify if such a correlation exists in other organisms as well, we analyzed organisms in which the organization and replication timing of the genome have already been studied. In ascomycete yeasts possessing the Rabl configuration of chromosomes, centromeres replicate early, and telomeres replicate late. Intriguingly, in maize, with a Rabl-like arrangement, the centromeres replicate in mid S-phase[53]. On the other hand, chromosomes in humans, chicken DT40 cells, and *A. thaliana* adopt the non-Rabl arrangement, and centromeres replicate during mid to late S in these organisms[30,39,54-57]. These observations raise an intriguing link between the spatial positioning of telomeres and centromeres in the nucleus and replication timing of these heterochromatic domains across kingdoms of life. Altogether, our study highlights the conformational plasticity of the *C. neoformans* genome and maps the structural changes associated with the Rabl and non-Rabl conformational switching during the cell cycle. Most importantly, the conformation-switching behavior of *C. neoformans* chromosomes makes it a unique model system for studying the factors responsible for shaping the genome architecture in organisms that lack condensin II and sheds light on the evolutionary diversity of the 3D genome architecture.

Acknowledgements

We thank members of the Sanyal laboratory for their support, discussion, and suggestions on the work. We thank R. Siddharthan, The Institute of Mathematical Sciences, Chennai, and L. Narlikar, IISER Pune, for the discussion and suggestions on the work. We thank V. Yadav, Duke University, for the discussion and comments on the manuscript. We thank K. Hardwick (University of Edinburgh) for the *MPS1* overexpression strain. We thank N. Nala and the in-house flow cytometry facility at JNCASR. We thank the NGS facility at NCBS and A. Pandit for sequencing Hi-C samples and for discussions on the DNA library preparation. This work was supported by the Anusandhan National Research Foundation (ANRF), Department of Science and Technology, Government of India (CRG/2023/001077) and intramural financial support from JNCASR to K.S. K.S. is a JC Bose National Fellow (JCB/2020/000021). S.D.P. acknowledges fellowship from ANRF (CRG/2023/001077), S.D. acknowledges fellowship support from the PMRF, Ministry of Education, India. R.P. acknowledges support from Sunita Sanghi Centre of Aging and Neurodegenerative Diseases (SCAN), IIT Bombay. The funders had no role in study design, data collection and analysis, decision to publish, or preparation of the manuscript.

Competing interests

The authors declare no competing interests.

References

1. Sakamoto, T. *et al.* Two-step regulation of centromere distribution by condensin II and the nuclear envelope proteins. *Nat Plants* **8**, 940-953 (2022).
2. Nathanailidou, P., Taraviras, S. & Lygerou, Z. Chromatin and nuclear architecture: shaping DNA replication in 3D. *Trends Genet* **36**, 967-980 (2020).
3. Muller, H., Gil, J., Jr. & Drinnenberg, I.A. The impact of centromeres on spatial genome architecture. *Trends Genet* **35**, 565-578 (2019).
4. Tjong, H. *et al.* Population-based 3D genome structure analysis reveals driving forces in spatial genome organization. *Proc Natl Acad Sci U S A* **113**, E1663-72 (2016).
5. Hoencamp, C. *et al.* 3D genomics across the tree of life reveals condensin II as a determinant of architecture type. *Science* **372**, 984-989 (2021).
6. Torres, D.E., Reckard, A.T., Klocko, A.D. & Seidl, M.F. Nuclear genome organization in fungi: from gene folding to Rabl chromosomes. *FEMS Microbiol Rev* **47**(2023).
7. Takahashi, K., Chen, E.S. & Yanagida, M. Requirement of Mis6 centromere connector for localizing a CENP-A-like protein in fission yeast. *Science* **288**, 2215-9 (2000).
8. Yadav, V. *et al.* Cellular Dynamics and Genomic Identity of Centromeres in Cereal Blast Fungus. *mBio* **10**(2019).
9. Marshall, W.F., Dernburg, A.F., Harmon, B., Agard, D.A. & Sedat, J.W. Specific interactions of chromatin with the nuclear envelope: positional determination within the nucleus in Drosophila melanogaster. *Mol Biol Cell* **7**, 825-42 (1996).
10. Bauer, C.R., Hartl, T.A. & Bosco, G. Condensin II promotes the formation of chromosome territories by inducing axial compaction of polyploid interphase chromosomes. *PLoS Genet* **8**, e1002873 (2012).
11. Rodrigues, A. *et al.* Nucleoli and the nucleoli-centromere association are dynamic during normal development and in cancer. *Mol Biol Cell* **34**, br5 (2023).
12. Jimenez-Martin, A. *et al.* Centromere positioning orchestrates telomere bouquet formation and the initiation of meiotic differentiation. *Nat Commun* **16**, 837 (2025).
13. Kozubowski, L. *et al.* Ordered kinetochore assembly in the human-pathogenic basidiomycetous yeast Cryptococcus neoformans. *mBio* **4**, e00614-13 (2013).
14. Sridhar, S., Hori, T., Nakagawa, R., Fukagawa, T. & Sanyal, K. Bridgin connects the outer kinetochore to centromeric chromatin. *Nat Commun* **12**, 146 (2021).
15. Baumann, P. & Cech, T.R. Pot1, the putative telomere end-binding protein in fission yeast and humans. *Science* **292**, 1171-5 (2001).
16. Jin, Q.W., Fuchs, J. & Loidl, J. Centromere clustering is a major determinant of yeast interphase nuclear organization. *J Cell Sci* **113 (Pt 11)**, 1903-12 (2000).
17. Guacci, V., Hogan, E. & Koshland, D. Centromere position in budding yeast: evidence for anaphase A. *Mol Biol Cell* **8**, 957-72 (1997).
18. Funabiki, H., Hagan, I., Uzawa, S. & Yanagida, M. Cell cycle-dependent specific positioning and clustering of centromeres and telomeres in fission yeast. *J Cell Biol* **121**, 961-76 (1993).
19. Solovei, I. *et al.* Differences in centromere positioning of cycling and postmitotic human cell types. *Chromosoma* **112**, 410-23 (2004).
20. Galazka, J.M. *et al.* Neurospora chromosomes are organized by blocks of importin alpha-dependent heterochromatin that are largely independent of H3K9me3. *Genome Res* **26**, 1069-80 (2016).
21. Mizuguchi, T. *et al.* Cohesin-dependent globules and heterochromatin shape 3D genome architecture in S. pombe. *Nature* **516**, 432-435 (2014).

22. Duan, Z. *et al.* A three-dimensional model of the yeast genome. *Nature* **465**, 363-7 (2010).
23. Yadav, V. *et al.* RNAi is a critical determinant of centromere evolution in closely related fungi. *Proc Natl Acad Sci U S A* **115**, 3108-3113 (2018).
24. Crane, E. *et al.* Condensin-driven remodelling of X chromosome topology during dosage compensation. *Nature* **523**, 240-4 (2015).
25. Abramo, K. *et al.* A chromosome folding intermediate at the condensin-to-cohesin transition during telophase. *Nat Cell Biol* **21**, 1393-1402 (2019).
26. Naumova, N. *et al.* Organization of the mitotic chromosome. *Science* **342**, 948-53 (2013).
27. Lieberman-Aiden, E. *et al.* Comprehensive mapping of long-range interactions reveals folding principles of the human genome. *Science* **326**, 289-93 (2009).
28. Rowley, M.J. *et al.* Evolutionarily conserved principles predict 3D chromatin organization. *Mol Cell* **67**, 837-852 e7 (2017).
29. Dong, P. *et al.* 3D chromatin architecture of large plant genomes determined by local A/B compartments. *Mol Plant* **10**, 1497-1509 (2017).
30. Rao, S.S. *et al.* A 3D map of the human genome at kilobase resolution reveals principles of chromatin looping. *Cell* **159**, 1665-80 (2014).
31. Dixon, J.R. *et al.* Topological domains in mammalian genomes identified by analysis of chromatin interactions. *Nature* **485**, 376-80 (2012).
32. Muller, C.A. & Nieduszynski, C.A. Conservation of replication timing reveals global and local regulation of replication origin activity. *Genome Res* **22**, 1953-62 (2012).
33. Koren, A., Soifer, I. & Barkai, N. MRC1-dependent scaling of the budding yeast DNA replication timing program. *Genome Res* **20**, 781-90 (2010).
34. Dumesic, P.A. *et al.* Product binding enforces the genomic specificity of a yeast polycomb repressive complex. *Cell* **160**, 204-18 (2015).
35. Raghuraman, M.K. *et al.* Replication dynamics of the yeast genome. *Science* **294**, 115-21 (2001).
36. Kim, S.M., Dubey, D.D. & Huberman, J.A. Early-replicating heterochromatin. *Genes Dev* **17**, 330-5 (2003).
37. Koren, A. *et al.* Epigenetically-inherited centromere and neocentromere DNA replicates earliest in S-phase. *PLoS Genet* **6**, e1001068 (2010).
38. Massey, D.J. & Koren, A. Telomere-to-telomere human DNA replication timing profiles. *Sci Rep* **12**, 9560 (2022).
39. Ten Hagen, K.G., Gilbert, D.M., Willard, H.F. & Cohen, S.N. Replication timing of DNA sequences associated with human centromeres and telomeres. *Mol Cell Biol* **10**, 6348-55 (1990).
40. Lazar-Stefanita, L. *et al.* Cohesins and condensins orchestrate the 4D dynamics of yeast chromosomes during the cell cycle. *EMBO J* **36**, 2684-2697 (2017).
41. Thakur, J. & Sanyal, K. A coordinated interdependent protein circuitry stabilizes the kinetochore ensemble to protect CENP-A in the human pathogenic yeast Candida albicans. *PLoS Genet* **8**, e1002661 (2012).
42. Guin, K. *et al.* Spatial inter-centromeric interactions facilitated the emergence of evolutionary new centromeres. *Elife* **9**(2020).
43. Torres, D.E. *et al.* Implications of the three-dimensional chromatin organization for genome evolution in a fungal plant pathogen. *Nat Commun* **15**, 1701 (2024).

44. Winter, D.J. *et al.* Repeat elements organise 3D genome structure and mediate transcription in the filamentous fungus Epichloe festucae. *PLoS Genet* **14**, e1007467 (2018).
45. Hsieh, T.H. *et al.* Mapping nucleosome resolution chromosome folding in yeast by Micro-C. *Cell* **162**, 108-19 (2015).
46. Yadav, V. & Sanyal, K. Sad1 spatiotemporally regulates kinetochore clustering to ensure high-Fidelity chromosome segregation in the human fungal pathogen Cryptococcus neoformans. *mSphere* **3**(2018).
47. Hirano, T. Condensins: universal organizers of chromosomes with diverse functions. *Genes Dev* **26**, 1659-78 (2012).
48. Hayashi, M.T., Takahashi, T.S., Nakagawa, T., Nakayama, J. & Masukata, H. The heterochromatin protein Swi6/HP1 activates replication origins at the pericentromeric region and silent mating-type locus. *Nat Cell Biol* **11**, 357-62 (2009).
49. Dave, A., Cooley, C., Garg, M. & Bianchi, A. Protein phosphatase 1 recruitment by Rif1 regulates DNA replication origin firing by counteracting DDK activity. *Cell Rep* **7**, 53-61 (2014).
50. Tazumi, A. *et al.* Telomere-binding protein Taz1 controls global replication timing through its localization near late replication origins in fission yeast. *Genes Dev* **26**, 2050-62 (2012).
51. Aparicio, O.M. Location, location, location: it's all in the timing for replication origins. *Genes Dev* **27**, 117-28 (2013).
52. Sreekumar, L. *et al.* Orc4 spatiotemporally stabilizes centromeric chromatin. *Genome Res* **31**, 607-621 (2021).
53. Wear, E.E. *et al.* Genomic analysis of the DNA replication timing program during mitotic S phase in Maize (Zea mays) root tips. *Plant Cell* **29**, 2126-2149 (2017).
54. Feng, S. *et al.* Genome-wide Hi-C analyses in wild-type and mutants reveal high-resolution chromatin interactions in Arabidopsis. *Mol Cell* **55**, 694-707 (2014).
55. Grob, S., Schmid, M.W. & Grossniklaus, U. Hi-C analysis in Arabidopsis identifies the KNOT, a structure with similarities to the flamenco locus of Drosophila. *Mol Cell* **55**, 678-93 (2014).
56. Concia, L. *et al.* Genome-wide analysis of the Arabidopsis replication timing program. *Plant Physiol* **176**, 2166-2185 (2018).
57. Shang, W.H. *et al.* Chromosome engineering allows the efficient isolation of vertebrate neocentromeres. *Dev Cell* **24**, 635-48 (2013).

Methods

Strains and media growth conditions

A list of strains and plasmids used in this study is available in Supplementary Table 1. *C. neoformans* cultures were grown and maintained on YPD media (1% yeast extract, 2% peptone, and 2% dextrose) and YPG (1% yeast extract, 2% peptone, and 2% galactose) at 30°C unless otherwise specified. YPD+1M sorbitol plates were used for the transformation of *C. neoformans* cells. Approximately 100 µg/mL of nourseothricin (NAT, clonNAT, Werner BioAgents) was used for the selection of transformants. The primers used in this study to prepare constructs for generating and confirming the desired strains are listed in Supplementary Table 2.

Biolistic transformation

Biolistic transformation was performed as described previously[1]. Briefly, an overnight-grown 5 mL culture of *C. neoformans* was harvested and resuspended in 300 µL of sterile dH_2O. The cell suspension was spread on a YPD+1M sorbitol plate and allowed to dry. Gold micro-carrier beads (0.6 µm) coated with 2-5 µg of DNA, resuspended in 100% ethanol, were placed on a micro-carrier disk and allowed to dry. Dried disks containing DNA-coated beads were bombarded onto plates containing *C. neoformans* cells using the Biolistic® PDS-1000/He Particle Delivery System. Cells were then plated on YPD+NAT selection plates and incubated at 30°C for 3-4 days for transformants to appear.

Construction of *GFP-POT1* tagged strains

The fluorescent fusion protein of Pot1 was generated by cloning the 1.48 kb upstream homology region and promoter of *POT1* into the pVY7 plasmid containing the GFP NAT sequence. GFP was tagged to the N-terminal region of the *POT1* gene. The primers used to generate the clones are listed in Supplementary Table 2. The 1.48 kb homology region and 0.56 kb *POT1* promoter region were amplified from the *POT1* gene using H99 genomic DNA. Individual PCR fragments were purified using gel electrophoresis. The amplified regions were cloned using SpeI, SacI, and NcoI. The final clone was linearized using StuII and transformed into the CNVY101 background. The obtained transformants were confirmed by PCR.

Fluorescence microscopy

For widefield microscopy, a Zeiss Axio Observer 7 equipped with a 100x Plan Apochromat 1.4 NA objective, Colibri 7 LED light source, motorized XYZ stage, and PCO.edge 4.2 sCMOS camera was used. Images were acquired at 4 × 4 binning. Zen blue edition (2.3) software was used to control the microscope components and acquisition. For Airyscan imaging, a Zeiss LSM 880 Axio Observer confocal microscope equipped with a solid-state laser light source, 100x Plan Apochromat 1.4 NA objective, motorized XYZ stage, and Airyscan module was used to obtain images. Airyscan detection system was used to acquire images for centromere and telomere localization. Zen software (black edition) was used to control the microscope and process the Airyscan raw images. The number of centromere and telomere foci in unbudded cells was estimated using Fiji[2].

Super-resolution (SR) imaging of centromere and telomere localization

For SR imaging, log-phase *C. neoformans* cells were fixed using 4% paraformaldehyde in 1x PBS (pH 7.4) and incubated at RT for 20 min. The fixed cells were washed twice with 1x PBS,

and 2µL of the cell suspension was placed on a microscope cover glass and imaged. For SR imaging, a Zeiss Elyra 7 lattice SIM[2] microscope equipped with a solid-state laser light source, Plan-Apochromat 63x 1.4 NA objective, motorized XYZ stage, and PCO.edge 4.2 sCMOS camera were used. Z-stack images were acquired using the leap mode at intervals of 0.11 µm. The raw images obtained were processed using the Zen software (Black Edition).

Elutriation

To isolate unbudded interphase[G1] cells, elutriation was performed using an Avanti J-26 XP (Beckman) in combination with a JE-5.0 elutriator rotor and a 40 mL elutriation chamber. The method was modified from[3] to suit the morphology of *C. neoformans* yeast cells. Log-phase asynchronous cell cultures were used for elutriation. An overnight-grown culture was used to inoculate 400 mL of 2% YPD at 0.05 OD_{600}/mL and grown overnight at 180 RPM, to reach 2.0 OD_{600}/mL. The following day, this culture was used to inoculate 2x 1 L YPD media (0.3 OD_{600}/mL) and was grown until ~ 1.5 OD_{600}/mL. The cultures were pelleted, washed twice with 1x PBS, and resuspended in 50 mL of 1x PBS. Clumped cells were resolved by sonication. Approximately 6×10^9 cells were pumped into the elutriation system at a flow rate of 14 mL/min and a rotor speed of 2500 rpm. Once the cells were loaded, equilibrium was achieved for 30 min, during which there was no output of cells from the chamber. To start eluting the unbudded G1 cells, the flow rate was gradually increased by 1 mL/min until the output became turbid. 1 L fractions of increasing flow rates were collected. The fraction containing unbudded cells was confirmed by FACS and microscopy and processed for Hi-C experiments.

Synchronization of cells at metaphase and anaphase

To obtain synchronous populations of metaphase and anaphase cells, the cells were first synchronized using hypoxia, which resulted in unbudded G2 arrest, as mentioned previously[4]. For metaphase arrest, hypoxia-synchronized cells were released by shifting to extensive aeration in YPGalactose (YPG) media to induce overexpression of Mps1. Mps1 has been shown to cause irreversible metaphase arrest in *C. neoformans*[5]. For the anaphase stage, hypoxia-synchronized cells were first arrested using thiabendazole (10 µg/mL) for 2 h, washed, and released into fresh YPD media. Synchrony was assessed using microscopy and flow cytometry.

Hi-C

This protocol was adapted and modified from previously published literature[6-8]. For Hi-C library preparation, approximately 50 OD_{600} cells from three stages were suspended in 2% YPD and fixed with formaldehyde (3% final concentration) for 20 min, then quenched with 125 mM glycine final concentration for another 20 min at room temperature. The fixed cells were washed and resuspended in 1x Tris buffer (50 mM Tris-HCl pH 7.5, and 150 mM NaCl) with protease inhibitor cocktail and lysed using a Bio-spec Bead Beater. The lysate was centrifuged, and the pellet was washed with 1x NEB DpnII buffer. The pellet was digested with DpnII, followed by 14 biotin-dCTP fill in (Jena Bioscience), ligation, decrosslinking, Phenol: Chloroform: Isoamyl alcohol purification, precipitation, and RNase treatment as mentioned in[6]. DNA was fragmented using a Covaris M220 focused ultrasonicator to produce fragments in the size range of 200–500 bp. Sheared DNA fragments were fractionated using AMpure XP beads and pulled down using MyOne Streptavidin C1 beads. On-bead DNA library preparation was performed using the NEBNext Ultra II DNA library preparation kit (E7645), as reported

previously[6]. The generated libraries were sequenced using 150-bp paired-end reads on an Illumina Novaseq 6000 machine (NGS facility, NCBS, Bengaluru, India). The Hi-C sequencing read statistics are listed in Supplementary Table 3.

Processing Hi-C data

Hi-C reads were aligned to the *C. neoformans H99* reference genome (ASM1180120v1)[9] and processed using the HiC-Pro (3.1.0) pipeline[10]. Fastq reads were mapped by Bowtie2[11] (2.3.5.1) using default parameters. Multiple hits, duplicates, and singletons were removed. The read pairs were assigned to the ligated restriction site DpnII, and invalid pairs were removed. Each replicate was processed independently, and the valid pairs were merged as one file and used for downstream analysis (refer to Supplementary Table 3 for read-pairing statistics). The valid pairs generated were converted to cool format and used to create balanced mcool files of resolutions 2, 4, 8, 16, and 32 kb using cooler[12]. Visual inspection of contact maps revealed structural changes associated with the genome of the strain used to generate the Hi-C maps. These regions were masked using cooler --blacklist option while generating balanced mcool files. The analyses presented in this paper were performed using replicate merged and masked mcool files.

Visualization of Hi-C contact maps

The Hi-C contact maps and observed/expected correlated maps were plotted with $\log_{10}$, $\log_{2,}$ and linear scales using the plotMatrix function from HiContacts[13] in R Studio 4.4.2.

Plotting *P(s)* curves

The *P(s)* curves were plotted using 2 kb binned Hi-C matrices. Using cooltools[14], *P(s)* for the chromosomal arms was estimated.

Calculation of eigen compartments

Eigenvalue decomposition of Hi-C matrices was performed using cooltools[14] at an 8 kb resolution. To determine compartment identity, the Pearson correlation between eigenvalues and gene density (computed over 8 kb windows for each chromosome) was calculated. The sign of each eigenvalue was adjusted based on this correlation: if the correlation was positive, the original sign was retained; if it was negative, the sign was inverted.

Aggregate maps of centromeres and telomeres

Aggregate maps of inter/intra-chromosomal contacts involving centromeres and telomeres were generated using the aggregate function of HiContacts[13]. For off-diagonal contacts (*trans* contacts), 200 kb regions surrounding centromeres and 200 kb regions from the ends of the chromosomes (telomeres) were used. Aggregate contact maps binned at 8 kb resolution were plotted. A total of 182 pair-wise combinations of centromere and telomere p-arm interactions were plotted as aggregate plots. For on-diagonal interactions (*cis*) of centromeres and telomeres, Hi-C matrices binned at 2 kb resolution were used, and the aggregates were plotted as observed/expected maps using the detrend function from HiContacts. Aggregate maps surrounding the centromeres and telomeres were generated using the aggregate function from HiContacts. 8 kb binned matrices were used for this analysis and plotted using plotMatrix.

Insulation score and domain calling

Insulation scores were calculated using FAN-C[15] on Hi-C matrices binned at 2 kb resolution using a 50 kb window. hicFindTADs[16] from HicExplorer was used to call the domains using a 2 kb binned Hi-C matrix of interphase[G1] stage using the following settings: --delta = 0.001, --minDepth 30000, --maxDepth 80000. The domains estimated using HicExplorer were aggregated across the genome using the FAN-C aggregate function and plotted as a heatmap (2 kb resolution). Hi-C contact maps, along with insulation profiles and domains, were plotted using PyGenomeTracks[17].

ChIP-seq data processing

The histone marks H3K27me3, H3K9me2, and control WCE ChIP-seq data used in the study were downloaded from GEO: GSE61550[18]. The raw sequence reads were aligned to the reference genome H99 using bowtie2[11]. The aligned files were sorted, duplicates were removed, and then sorted using samtools[19]. The ChIP-seq bam files were normalized to the sequencing depth. The log2 enrichment over control ChIP-seq data was then calculated for both histone mark data to generate bedGraph files over a window of 50 and 1000 bp using deepTools[20].

RNA-seq

RNA-seq data of G1 stage cells (0 min time point, post-elutriation released cells) were obtained from GEO: GSE80474[21]. The raw reads were aligned using the STAR rna-seq[22] aligner to the reference genome H99, and the respective aligned and sorted bam files were used to compare the gene expression patterns in the genome compartments.

Circos plots

Circos plots were generated using the Circos tool[23]. Hi-C data were processed using cooltools and HiCExplorer for analysis. Highly enriched 3D chromatin interactions (log2 ratio observed to the expected >3) are plotted as links. The eigenvalues were calculated using cooltools and are shown as separate tracks in the plot. The chip enrichment signal of histone modifications, that is, H3K27me3 and H3K9me2 over the control sample, is shown as two different tracks in the figure. Replication timing data are shown as another track in the plot.

Sort-seq

The protocol was adapted from a previously published report[24] with the following modifications. For sorting G1 and S phase cells, an overnight grown culture of *H99* cells was inoculated at 0.2 $O.D_{600}$/mL and grown for 5 h until the OD_{600} reached 1. Approximately 20 O.D cells were washed twice with sterile water, fixed using 70% ethanol at room temperature for 1 h, and subsequently incubated overnight at 4°C. The cells were pelleted and washed twice with NS buffer (10 mM Tris-HCl pH 7.5, 250 mM sucrose, 1 mM EDTA (pH 8.0), 1 mM $MgCl_2$, 0.1 mM $CaCl_2$, and 7 mM β-mercaptoethanol). The cells were resuspended in 10 mL of NS buffer, treated with RNase A, washed with 1x PBS and stained with propidium iodide (PI) (HiMedia, Mumbai, India). The suspension was then incubated overnight in the dark at 4 °C. Before sorting, the stained samples were sonicated and sorted using FACSAria III (BD Biosciences). Approximately 15 million G1 and 10 million S phase cells were collected. As a control, 5 million total G1, S, and G2 cells were collected. The sorted cells were analyzed for purity (Extended Data Fig. 10 and Supplementary Figure 1). Genomic DNA was isolated from both G1 and S phase cells using the bead beating method, subjected to library preparation

using an Illumina kit, and the libraries generated were sequenced using 150-bp paired-end reads on the Illumina Nova-seq 6000 machine at Clevergene Inc., Bengaluru, India.

The Fastq files of the G1 and S phase samples were mapped using the Repliscope pipeline (https://github.com/DNAReplicationLab/Repliscope) with a few modifications. Briefly, the Fastq files were aligned using bowtie2 in paired-end and local modes, and the reads were binned using a 1000 bp window. Reads mapped more than once were not removed from the analysis by setting the MapQ threshold to 3 to include centromeric reads for downstream analysis. As reported previously[24-26], the read depth adjusted S/G1 ratio was calculated using makeRatio function of Repliscope, and the data were normalized to zero mean and 1 standard deviation, resulting in z-scores where values above and below zero indicate early and late replicating regions, respectively. The profiles were plotted using R Studio 4.4.2.

Polymer simulation of individual chromosomes and the whole genome

Individual chromosomes are composed of N_i beads, each of size 10 kb and diameter σ. Intra-chromosomal beads (i and j) are constrained to be in contact with probability P_{ij} as reported in[27]. This was achieved in two steps, where the first step involved contact formation among the prominent contacts, followed by contact formation among all beads. After generating ensembles of 1000 polymer structures for each of the 14 chromosomes, ensuring that they accurately reproduced the experimentally observed intrachromosomal contact patterns, randomly selected configurations for each chromosome were placed together within a spherical confinement that mimicked the nuclear environment. Based on microscopy imaging of fluorescently tagged H4, the nuclear volume was set to approximately $4.29\,\mu\mathrm{m}^3$, which corresponds to a nuclear radius of about $1\,\mu\mathrm{m}$ under the assumption of a spherical shape. The radius of the spherical confinement was set to 14σ, where $\sigma \approx 71.4\ \mathrm{nm}$. This choice of σ yielded a confinement radius that matched the experimental nuclear size. The resulting chromatin volume fraction inside the nucleus is,

$$\frac{1914 \cdot \frac{4}{3}\pi(\sigma/2)^3}{\frac{4}{3}\pi(14\sigma)^3} = 0.087,$$

where 1914 is the total number of beads. This volume fraction was in good agreement with the typical chromatin density observed in the nucleus[28]. The nuclear peripheral localization behaviour of centromeres and telomeres was incorporated into the model, using an attractive Lennard-Jones (LJ) interaction between the nuclear wall and both centromeres and telomeres, defined as:

$$E_{LJ}(r) = \begin{cases} 4\epsilon\left[\left(\frac{\sigma}{r}\right)^{12} - \left(\frac{\sigma}{r}\right)^{6}\right], & r < 2.5\sigma \\ 0, & r \geq 2.5\sigma \end{cases}$$

Here, r is the distance between any pair of interacting beads. While simulating wall-centromere, wall-telomeres, centromere-centromere ($\mathrm{cen}-\mathrm{cen}$) and telomere-telomere interactions ($\mathrm{tel}-\mathrm{tel}$), we took $\epsilon = \epsilon_{\mathrm{WC}}$ $\epsilon = \epsilon_{\mathrm{WT}}$, $\epsilon = \epsilon_{\mathrm{CC}}$ and $\epsilon = \epsilon_{\mathrm{TT}}$ respectively. All other beads interact via purely repulsive excluded volume interactions, where E_{LJ} acts only where $\mathrm{r} < 2^{(1/6)}\,\sigma$.

From Hi-C data, we estimated the strong and weak interactions associated with centromeres and telomeres, and we accordingly tuned ϵ parameters and obtained configurations that are consistent with microscopy observations. Once the parameters are finalized, the system is equilibrated using Langevin dynamics simulations implemented in LAMMPS[29]. Here, we solved the Langevin equation with the above-mentioned interactions and thermal fluctuations.

Calculation of distal contact index (DCI)

To compare contact maps across different stages of the cell cycle and quantitatively understand how contact patterns vary, the Distal Contact Index (DCI) was computed[30]. The (normalized) local contact signal $C_l(i)$ and distal contact signal $C_d(i)$ were defined for each chromatin bin i as:

$$C_l(i) = \frac{1}{N_l(i)} \sum_{j=1}^{N} P_{ij}\, \Theta(s_d - s_{ij}),$$

$$C_d(i) = \frac{1}{N_d(i)} \sum_{j=1}^{N} P_{ij}\, \Theta(s_{ij} - s_d),$$

where P_{ij} denotes the contact probability between chromatin segments in bins i and j, and s_{ij} represents their genomic separation. The terms $N_l(i)$ and $N_d(i)$ denote the number of possible local and distal contact pairs, respectively, for bin i. The genomic distance threshold s_d defines the boundary between local and distal contacts. We set $s_d = 70$ kb, based on the maximum domain size observed (Extended Fig. data 6). Contacts beyond this threshold are considered distal or nonlocal. Using the above definitions, the DCI for bin i was computed as:

$$\mathrm{DCI}(i) = \log\left(\frac{C_d(i)}{C_l(i)}\right).$$

DCI is not well-defined in genomic regions that are difficult to sequence and lack reliable contact signals, such as the centromeric regions. A higher DCI value for a bin i indicates the presence of contacts beyond typical domain sizes, which may signify the formation of long-range chromatin interactions.

Calculation of compaction profiles

The polymer radius of gyration is a conventional measure of compaction; alternatively, compaction can be defined based on contact matrices. Intuitively, higher compaction corresponds to higher contact probability values among genomic regions.

The average compaction $\langle P(k) \rangle$ of the k-th bin is defined as the mean contact probability within a symmetric window centered at k, of width w,

$$\langle P(k) \rangle = \frac{1}{N_w} \sum_{i=k-w/2}^{k+w/2} \sum_{j=k-w/2, j\neq i}^{k+w/2} P_{ij}$$

where N_w is the number of non-diagonal terms.

Radius of gyration and asphericity

Chromosome shape characteristics, such as the radius of gyration and asphericity, were quantified using the gyration tensor. By calculating the eigenvalues of the gyration tensor (λ_1, λ_2, and λ_3), we derived the following shape descriptors:

$$\text{Radius of gyration (Rg)} = \sqrt{\sum_i \lambda_i}$$

$$\text{Asphericity} = \frac{3}{2}\left(\frac{\sum_i (\lambda_i - \overline{\lambda})^2}{(\sum_i \lambda_i)^2}\right)$$

where $\overline{\lambda}$ is the average of all eigen-values. Asphericity quantifies the deviation of the shape from a perfect sphere; it is zero for a sphere and increases as the shape deviates from that of a sphere.

Polymer model visualization

The simulation configuration snapshot images were visualized using the mol* viewer[31].

References

1. Davidson, R.C. *et al.* Gene disruption by biolistic transformation in serotype D strains of Cryptococcus neoformans. *Fungal Genet Biol* **29**, 38-48 (2000).
2. Schindelin, J. *et al.* Fiji: an open-source platform for biological-image analysis. *Nat Methods* **9**, 676-82 (2012).
3. Marbouty, M., Ermont, C., Dujon, B., Richard, G.F. & Koszul, R. Purification of G1 daughter cells from different Saccharomycetes species through an optimized centrifugal elutriation procedure. *Yeast* **31**, 159-66 (2014).
4. Polisetty, S.D. *et al.* The dependence of shugoshin on Bub1-kinase activity is dispensable for the maintenance of spindle assembly checkpoint response in Cryptococcus neoformans. *PLoS Genet* **21**, e1011552 (2025).
5. Aktar, K. *et al.* Conserved signalling functions for Mps1, Mad1 and Mad2 in the Cryptococcus neoformans spindle checkpoint. *PLoS Genet* **20**, e1011302 (2024).
6. Golloshi, R., Sanders, J.T. & McCord, R.P. Iteratively improving Hi-C experiments one step at a time. *Methods* **142**, 47-58 (2018).
7. Rao, S.S. *et al.* A 3D map of the human genome at kilobase resolution reveals principles of chromatin looping. *Cell* **159**, 1665-80 (2014).
8. Belaghzal, H., Dekker, J. & Gibcus, J.H. Hi-C 2.0: An optimized Hi-C procedure for high-resolution genome-wide mapping of chromosome conformation. *Methods* **123**, 56-65 (2017).
9. Yadav, V., Sun, S., Coelho, M.A. & Heitman, J. Centromere scission drives chromosome shuffling and reproductive isolation. *Proc Natl Acad Sci U S A* **117**, 7917-7928 (2020).
10. Servant, N. *et al.* HiC-Pro: an optimized and flexible pipeline for Hi-C data processing. *Genome Biol* **16**, 259 (2015).
11. Langmead, B. & Salzberg, S.L. Fast gapped-read alignment with Bowtie 2. *Nat Methods* **9**, 357-9 (2012).
12. Abdennur, N. & Mirny, L.A. Cooler: scalable storage for Hi-C data and other genomically labeled arrays. *Bioinformatics* **36**, 311-316 (2020).
13. Serizay, J., Matthey-Doret, C., Bignaud, A., Baudry, L. & Koszul, R. Orchestrating chromosome conformation capture analysis with Bioconductor. *Nat Commun* **15**, 1072 (2024).
14. Open2C *et al.* Cooltools: Enabling high-resolution Hi-C analysis in Python. *PLoS Comput Biol* **20**, e1012067 (2024).
15. Kruse, K., Hug, C.B. & Vaquerizas, J.M. FAN-C: a feature-rich framework for the analysis and visualisation of chromosome conformation capture data. *Genome Biol* **21**, 303 (2020).
16. Ramirez, F. *et al.* High-resolution TADs reveal DNA sequences underlying genome organization in flies. *Nat Commun* **9**, 189 (2018).
17. Lopez-Delisle, L. *et al.* pyGenomeTracks: reproducible plots for multivariate genomic datasets. *Bioinformatics* **37**, 422-423 (2021).
18. Dumesic, P.A. *et al.* Product binding enforces the genomic specificity of a yeast polycomb repressive complex. *Cell* **160**, 204-18 (2015).
19. Danecek, P. *et al.* Twelve years of SAMtools and BCFtools. *Gigascience* **10**(2021).
20. Ramirez, F. *et al.* deepTools2: a next generation web server for deep-sequencing data analysis. *Nucleic Acids Res* **44**, W160-5 (2016).

21. Kelliher, C.M., Leman, A.R., Sierra, C.S. & Haase, S.B. Investigating conservation of the cell-cycle-regulated transcriptional program in the fungal pathogen, Cryptococcus neoformans. *PLoS Genet* **12**, e1006453 (2016).
22. Dobin, A. *et al.* STAR: ultrafast universal RNA-seq aligner. *Bioinformatics* **29**, 15-21 (2013).
23. Krzywinski, M. *et al.* Circos: an information aesthetic for comparative genomics. *Genome Res* **19**, 1639-45 (2009).
24. Batrakou, D.G., Muller, C.A., Wilson, R.H.C. & Nieduszynski, C.A. DNA copy-number measurement of genome replication dynamics by high-throughput sequencing: the sort-seq, sync-seq and MFA-seq family. *Nat Protoc* **15**, 1255-1284 (2020).
25. Yehuda, Y., Blumenfeld, B., Lehmann, D. & Simon, I. Genome-wide determination of mammalian replication timing by DNA content measurement. *J Vis Exp* (2017).
26. Koren, A. *et al.* Differential relationship of DNA replication timing to different forms of human mutation and variation. *Am J Hum Genet* **91**, 1033-40 (2012).
27. Kadam, S. *et al.* Predicting scale-dependent chromatin polymer properties from systematic coarse-graining. *Nat Commun* **14**, 4108 (2023).
28. Brahmachari, S., Contessoto, V.G., Di Pierro, M. & Onuchic, J.N. Shaping the genome via lengthwise compaction, phase separation, and lamina adhesion. *Nucleic Acids Res* **50**, 4258-4271 (2022).
29. Thompson, A.P. *et al.* LAMMPS - a flexible simulation tool for particle-based materials modeling at the atomic, meso, and continuum scales. *Computer Physics Communications* **271**, 108171 (2022).
30. Chiang, M. *et al.* Polymer Modeling Predicts Chromosome Reorganization in Senescence. *Cell Rep* **28**, 3212-3223 e6 (2019).
31. Sehnal, D. *et al.* Mol* Viewer: modern web app for 3D visualization and analysis of large biomolecular structures. *Nucleic Acids Res* **49**, W431-W437 (2021).